High-Resolution Soil Moisture Retrieval With ASCAT

David B. Lindell, *Student Member, IEEE*, and David G. Long, *Fellow, IEEE*

***Abstract*—Satelliteborne C-band scatterometer measurements of the radar backscatter coefficient (σ^0) of the Earth can be used to estimate soil moisture levels over land. Such estimates are currently produced at 25- and 50-km resolution using the Advanced Scatterometer (ASCAT) sensor and a change detection algorithm originally developed at the Vienna University of Technology (TU-Wien). Using the ASCAT spatial response function (SRF), high-resolution (approximately 15–20 km per pixel) images of σ^0 can be produced, enabling the creation of a high-resolution soil moisture product using a modified version of the TU-Wien algorithm. The high-resolution soil moisture images are compared to images produced with the Water Retrieval Package 5.5 algorithm, which is also based on the TU-Wien algorithm, and to *in situ* measurements from the National Oceanic and Atmospheric Administration U.S. Climate Reference Network (NOAA CRN). The WARP 5.5 and high-resolution image products generally show good agreement with each other; the high-resolution estimates appear to resolve soil moisture features at a finer scale and demonstrate a tendency toward greater moisture values in some areas. When compared to volumetric soil moisture measurements from NOAA CRN stations for 2010 and 2011, the WARP 5.5 and high-resolution soil moisture estimates perform similarly, with both having a root-mean-square difference from the *in situ* data of approximately 0.06 m^3/m^3 in one study area and 0.09 m^3/m^3 in another.**

***Index Terms*—Advanced Scatterometer (ASCAT), scatterometer, soil moisture.**

I. Introduction

THE National Research Council's Decadal Survey emphasizes the importance of soil moisture measurements, citing their significance in predicting natural hazards and the role of soil moisture levels in the water and carbon cycles [1]. Soil moisture estimates are used for a variety of applications including drought detection, flood and landslide forecasts, crop yield monitoring, and rain precipitation models [1]–[5].

Various algorithms have been devised to use active and passive spaceborne sensors to estimate soil moisture levels [6]–[9], and ground-based *in situ* measurements are available in many locations for data validation [9], [10]. Due to the properties of spaceborne active C-band sensors, moisture can only be measured in the top few centimeters of the soil [11]. Orbiting sensors, however, can provide near-global estimates of soil moisture every few days. These sensors are generally able to measure soil moisture parameters despite cloud coverage and, in some cases, vegetation coverage of the target area.

Both 25- and 50-km resolution global soil moisture products are presently being produced using a change detection algorithm developed at the Vienna University of Technology (TU-Wien) [9], [12]. The products are processed using the Water Retrieval Package (WARP) algorithm with data from the C-band Advanced Scatterometer (ASCAT) sensors aboard the MetOp-A and MetOp-B satellites [10]. To produce an improved resolution product, we use the AVE algorithm [13] to create higher resolution images (approximately 15–20 km [13]) of the radar backscatter coefficient (σ^0). Exploiting ASCAT's high-resolution image capability enables higher resolution images of soil moisture than are currently available. By resolving finer soil moisture features, the higher resolution soil moisture images could complement soil moisture-related studies in such areas as crop yield prediction, drought prediction and localization, and modeling of the water table and water cycle [1]. This letter describes how the TU-Wien algorithm can be adapted to create high-resolution soil moisture images with ASCAT.

Interest in soil moisture retrieval has prompted the development and launch of satellite sensors designed primarily for soil moisture monitoring. For example, the ESA's Soil Moisture and Ocean Salinity sensor and NASA's Soil Moisture Active Passive sensor are specifically designed to provide accurate soil moisture estimates at reasonable spatial resolutions (approximately 50 and 9 km) [14], [15]. When compared with ASCAT, such sensors can provide more accurate measurements of soil moisture in certain areas, especially arid regions [16]. However, comparison studies generally show that ASCAT soil moisture products provide a consistent well-calibrated record [16], [17]. Although other sensors are perhaps better suited to soil moisture monitoring the high-resolution ASCAT estimates can be used to form a consistent soil moisture data record over a long period of time [8]. Such a record can be continued far into the future using the next iterations of the ASCAT sensor, launched on the MetOp-B satellite in 2012 and to be launched on the MetOp-C satellite in 2018.

The remainder of this letter is organized as follows. Section II provides a background, Section III discusses the implementation of an adapted TU-Wien algorithm, Section IV provides results, and Section V concludes.

II. Background

Data collected from both ASCAT and the European Remote-sensing Satellite (ERS) C-band scatterometers have been used to estimate relative soil moisture levels at 25 and 50 km per pixel resolution by applying the TU-Wien change detection algorithm to reported σ^0 values [8], [9]. This change detection

Manuscript received December 15, 2015; revised March 24, 2016; accepted April 18, 2016. Date of publication May 6, 2016; date of current version June 10, 2016.

The authors are with the Microwave Earth Remote Sensing Laboratory, Brigham Young University, Provo, UT 84602 USA (e-mail: lindell@mers.byu.edu; long@ee.byu.edu).

Color versions of one or more of the figures in this paper are available online at http://ieeexplore.ieee.org.

Digital Object Identifier 10.1109/LGRS.2016.2557321

algorithm exploits the dependence of σ^0 on soil moisture levels: in general, σ^0 increases as the amount of moisture in the soil increases [9]. The relative soil moisture in a particular area can be estimated by first normalizing all σ^0 values to a nominal incidence angle. Then, the maximum and minimum backscatter measurements are found from a long time series of data collected from the area under study. An assumption is made that the highest backscatter value in the time series corresponds to soil which is saturated with water and the lowest backscatter value corresponds to dry soil. For a given backscatter measurement, a relative soil moisture value (between 0% and 100%) is found by examining where the measurement falls between the measurements corresponding to dry and water-saturated soil. The volume content of moisture in the soil can also be extracted by multiplying the relative soil moisture value by the porosity of the soil [9]. In this way, a quantitative estimate of soil moisture can be produced using only σ^0 measurements.

The TU-Wien algorithm is briefly summarized here. The relative soil moisture is estimated by first normalizing the σ^0 values to incidence angles which reduce the effect of vegetation growth on the soil moisture estimates. At incidence angles of 25° $(\theta_{\rm dry})$ for dry soil and 40° $(\theta_{\rm wet})$ for wet soil, the backscatter from an undeveloped vegetation canopy is roughly equivalent to the backscatter from a developed vegetation canopy in a variety of climates [11].

As the relationship between σ^0 and the incidence angle is relatively unaffected by changes in soil moisture [18], the local backscatter values from a wide range of incidence angles are normalized to incidence angles of $\theta_{\rm dry}$ and $\theta_{\rm wet}$ and used to construct time series of measurements. The backscatter values are normalized as

$$\sigma^0(\theta_n,t)=\sigma^0(\theta,t)-\sigma^{0'}(\theta_n,t)(\theta-\theta_n)-\frac{1}{2}\sigma^{0''}(\theta_n)(\theta-\theta_n)^2 \quad (1)$$

where the first and second derivatives of σ^0 with respect to the incidence angle are given by $\sigma^{0'}$ and $\sigma^{0''}$, θ is the incidence angle of a particular measurement, and θ_n is either $\theta_{\rm dry}$ or $\theta_{\rm wet}$ [10].

The values of $\sigma^{0'}$ and $\sigma^{0''}$ over a given area are calculated using measurements from each ASCAT beam (fore, mid, and aft). Within a short temporal window, the separate beams observe each area within their collective swath at different incidence angles; hence, an estimate of $\sigma^{0'}$ can be calculated as

$$\sigma^{0'}\left(\frac{\theta_m-\theta_{a/f}}{2}\right)=\frac{\sigma^0_m(\theta_m)-\sigma^0_{a/f}\left(\theta_{a/f}\right)}{\theta_m-\theta_{a/f}} \quad (2)$$

where the m subscript indicates the midbeam measurement and the a/f subscript indicates either the aft beam or the fore beam measurement. The value of $\sigma^{0''}$ is estimated by calculating the slope of a regression line fit to the estimates of $\sigma^{0'}$ given at a range of incidence angles over some time window.

As described by Naeimi *et al.* [10], the time series of estimates of $\sigma^{0'}$ and $\sigma^{0''}$ are parameterized as

$$\sigma^{0'}(40,t)=C'+D'\Psi'(t) \quad (3)$$
$$\sigma^{0''}(40,t)=C''+D''\Psi''(t). \quad (4)$$

Here, C' and D' are parameters describing the minimum value and maximum range of the slope $\sigma^{0'}$, and C'' and D'' describe the minimum value and maximum range of the curvature $\sigma^{0''}$. The seasonal variations of the slope and curvature in a time series are described by empirically determined trigonometric functions Ψ' and Ψ'' [10].

The backscatter values corresponding to dry soil $(\sigma^0_{\rm dry})$ and wet soil $(\sigma^0_{\rm wet})$ at 40° incidence angle are found using the following equations:

$$\sigma^0_{\rm dry}(40,t)=C^0_{\rm dry}-D'\Psi'(t)(\theta_{\rm dry}-40)-\frac{1}{2}D''\Psi''(t)(\theta_{\rm dry}-40)^2 \quad (5)$$
$$\sigma^0_{\rm wet}(40,t)=C^0_{\rm wet}-D'\Psi'(t)(\theta_{\rm wet}-40)-\frac{1}{2}D''\Psi''(t)(\theta_{\rm wet}-40)^2. \quad (6)$$

Here, $C^0_{\rm dry}$ and $C^0_{\rm wet}$ correspond to the averaged lowest and highest observed values of backscatter in the time series where $\sigma^0(\theta_{inc})$ has been normalized to $\sigma^0(\theta_{\rm dry})$ and $\sigma^0(\theta_{\rm wet})$, respectively, [10], [11]. Note that $\sigma^0_{\rm wet}$ is equal to $C^0_{\rm wet}$ because 40° is chosen for $\theta_{\rm wet}$.

The relative topsoil moisture (m_s) for a given σ^0 measurement can be calculated using $\sigma^0_{\rm wet}$ and $\sigma^0_{\rm dry}$ and is given by

$$m_s(t)=\frac{\sigma^0(t)-\sigma^0_{\rm dry}(t)}{\sigma^0_{\rm wet}(t)-\sigma^0_{\rm dry}(t)}. \quad (7)$$

The m_s value is an estimate of the water saturation in the top few centimeters of the soil and takes on values between 0% and 100% [11].

III. High-Resolution Soil Moisture Retrieval

The process for creating high-resolution soil moisture estimates involves first creating high-resolution σ^0 images using the AVE algorithm, which is shown to have an effective resolution of approximately 15–20 km when used with ASCAT [13]. Then, an adapted form of the TU-Wien algorithm is applied to extract the soil moisture estimation parameters on a 4.45 by 4.45 km/pixel grid, which is a standard grid size for ASCAT AVE products [19]. In the adapted TU-Wien algorithm, a time series of σ^0 measurements for each pixel is normalized to incidence angles of $\theta_{\rm dry}$ and $\theta_{\rm wet}$ and evaluated to obtain the parameters $C^0_{\rm dry}$ and $C^0_{\rm wet}$. A correction is applied to compensate for an underestimation of $C^0_{\rm wet}$ in arid regions, and $\sigma^0_{\rm dry}$ and $\sigma^0_{\rm wet}$ are calculated using modified versions of (5) and (6). The relative topsoil moisture m_s is estimated on the 4.45 by 4.45 km/pixel grid.

The high-resolution C-band images of σ^0 are developed separately for the fore, mid, and aft beams of ASCAT using the AVE algorithm on ASCAT data from 2009 to 2014; six years of data is assumed to result in a time series of adequate length to estimate soil moisture. The AVE algorithm is an image reconstruction technique which uses the SRF of the scatterometer to identify the contribution of each area of the ground footprint of the sensor to a measured σ^0 value [13]. Each pixel in the reconstructed image is formed by taking an average of all σ^0 measurement values, weighted by the SRF value [13], [20].

Due to the fan beam geometry of the ASCAT sensor, σ^0 is measured at a range of incidence angles across the swaths of the fore, mid, and aft beams. When constructing the ASCAT AVE images for each beam, the effect of the variation in incidence angle is preserved across the measurement swaths. Where the swaths of the three beams overlap, three observations of σ^0 at different incidence angles are available. Using these

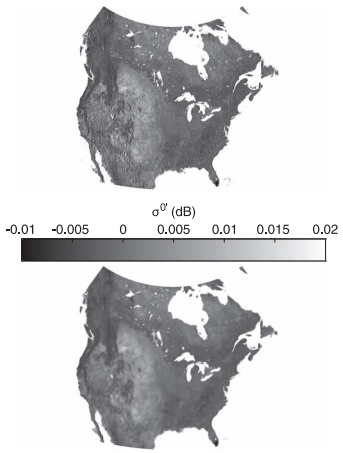

Fig. 1. Images of $\sigma^{0''}$ over North America for day 201, 2009 prior to median filtering (top) and after median filtering (bottom). Note that the moiré pattern present in the top image is removed by the median filter.

measurements, the first-order slope $(\sigma^{0'})$ and second-order slope $(\sigma^{0''})$ of σ^0 versus incidence angle can be calculated.

In order to reduce noise effects while preserving temporal variation, $\sigma^{0'}$ values are calculated for each pixel using (2) and a moving window of 30 days of data. To estimate the value of $\sigma^{0'}$ at 40° incidence angle, estimates of $\sigma^{0'}$ near 40° incidence angle are averaged. The value of $\sigma^{0''}$ is estimated by calculating the slope of a regression line fit to all estimates of $\sigma^{0'}$ from within the 30-day window for each pixel.

Unfortunately, images of $\sigma^{0''}$ contain artifacts where measurements from swath edges of separate orbital passes overlap. To suppress such artifacts, a median filter is applied to the $\sigma^{0''}$ images. Fig. 1 demonstrates the effect of the median filter on a sample image of $\sigma^{0''}$ from day 201, 2009. The image artifacts are removed in the median filtered image, and some finer details in the unfiltered image may also be removed.

The AVE σ^0 images are normalized to 25° $(\theta_{\rm dry})$ and 40° $(\theta_{\rm wet})$ incidence angles using (1) with the $\sigma^{0'}$ and median-filtered $\sigma^{0''}$ values. The normalized images from the fore, mid, and aft beams are combined using a weighted average of the pixel values, where the weighting is determined by the number of measurements from the original AVE reconstruction which contributed to each pixel value.

A time series of σ^0 $(\theta_{\rm dry})$ and σ^0 $(\theta_{\rm wet})$ values is constructed for each land pixel of the combined-beam images, and the parameters $C^0_{\rm dry}$ and $C^0_{\rm wet}$ are estimated. Following the WARP version 4 method of ASCAT m_s retrieval [10], $\sigma^0(\theta_{\rm dry})$ and $\sigma^0(\theta_{\rm wet})$ time series outlier values falling beyond three times the interquartile range from the mean are discarded. An average of the remaining σ^0 values is taken, and all values falling beyond 1.5 times the interquartile range are discarded. An average of the remaining lowest $\sigma^0(\theta_{\rm dry})$ and highest $\sigma^0(\theta_{\rm wet})$ values is assumed to correspond to dry and water-saturated soil moisture conditions over the land area associated with each pixel. For each pixel, the averaged high and low backscatter values are $C^0_{\rm dry}$ and $C^0_{\rm wet}$.

The sensitivity of the algorithm to soil moisture changes C^s can be observed by normalizing the $C^0_{\rm dry}$ values to a 40° incidence angle [using (1)] and taking the difference between $C^0_{\rm wet}$ and $C^0_{{\rm dry},40^\circ}$. In general, C^s decreases as vegetation cover increases and is greatest in areas of thin vegetation or bare soil

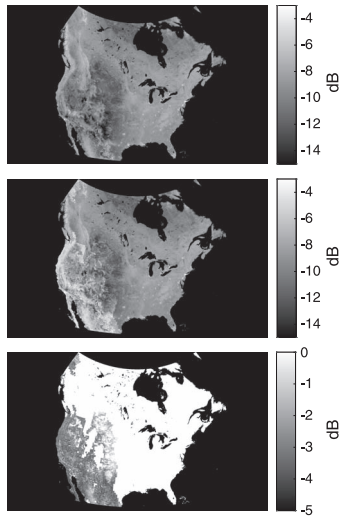

Fig. 2. Series of images showing initial $\sigma^0_{\rm wet}$ values (top), the corrected $\sigma^0_{\rm wet}$ values (middle), and the difference (bottom).

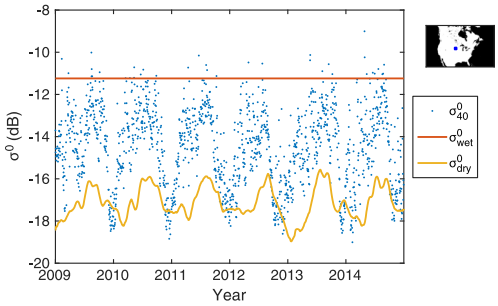

Fig. 3. Time series of $\sigma^0_{\rm wet}$, $\sigma^0_{\rm dry}$, and σ^0 for the pixel indicated in the map of North America in the upper right. Measurements of σ^0 approaching $\sigma^0_{\rm dry}$ (bottom line) are assumed to correspond to dry soil, whereas measurements approaching $\sigma^0_{\rm wet}$ (top line) are assumed to correspond to wet soil.

[11]. In areas of very heavy vegetation, $C^0_{\rm dry}$ increases, and C^s decreases, making classification less effective. Despite the lack of vegetation in especially arid or desert areas, values of $C^0_{\rm wet}$ are much lower than in other sparsely vegetated wetter regimes, contributing to an especially low C^s. The decreased sensitivity in dry regimes likely results from an absence of σ^0 measurements from water-saturated soil. Such low-biased $C^0_{\rm wet}$ values lead to an underestimation of $\sigma^0_{\rm wet}$.

Low $C^0_{\rm wet}$ values are identified using a map of climate regimes to isolate areas with an arid climate classification [21]. Following Naeimi *et al.* [10], a correction is applied in such areas by increasing $C^0_{\rm wet}$ until C^s is at least 5 dB. Differences between initial $C^0_{\rm wet}$ values and the corrected values over North America can be seen in Fig. 2. The majority of the corrections correspond to dry arid regions in the southwestern U.S. and Mexico.

The values of $\sigma^0_{\rm dry}$ and $\sigma^0_{\rm wet}$ are calculated by normalizing $C^0_{\rm dry}$ and $C^0_{\rm wet}$ from incidence angles of $\theta_{\rm dry}$ and $\theta_{\rm wet}$ to a 40° incidence angle using (1). In this case, $\theta_{\rm wet}$ is chosen to be 40° [10], so $C^0_{\rm wet}$ is equivalent to $\sigma^0_{\rm wet}$ and does not vary temporally. The $\sigma^0_{\rm dry}$ estimates vary over time and are smoothed to reduce the effects of noise. An example time series of $\sigma^0_{\rm wet}$, $\sigma^0_{\rm dry}$, and σ^0 for a single pixel is shown in Fig. 3. The figure shows the seasonal variation of σ^0 as well as where $\sigma^0_{\rm wet}$ and $\sigma^0_{\rm dry}$ are located with respect to the highest and lowest observed values of σ^0. Using the values calculated for $\sigma^0_{\rm dry}$ and $\sigma^0_{\rm wet}$, m_s is found using (7).

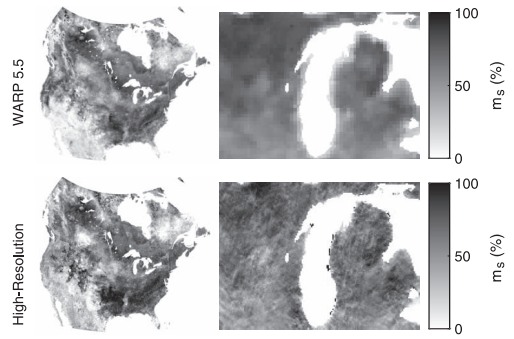

Fig. 4. Series of images comparing the high-resolution and WARP low-resolution m_s values using data from day of year (DOY) 121 to 125, 2009. The high-resolution image reveals finer features than the WARP image but reports greater soil moisture values than WARP in the southern U.S.

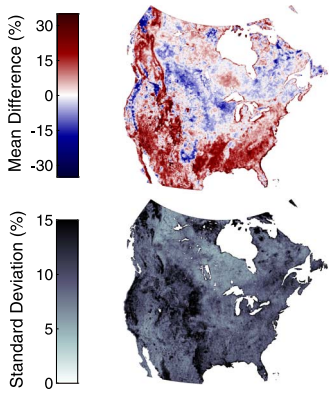

Fig. 5. Mean (left) and standard deviation (right) of the pixel value differences between the high-resolution and WARP low-resolution m_s estimates over a time series of images for 2009 for North America.

IV. Results

The high-resolution m_s estimates are compared to the 25-km resolution WARP 5.5 soil moisture product and *in situ* data from monitoring stations in the National Oceanic and Atmospheric Administration Climate Reference Network (NOAA CRN) [22], [23]. Data from the WARP soil moisture product are obtained from the EUMETSAT Satellite Application Facility on Support to Operational Hydrology and Water Management (H-SAF) data center and placed on a 12.5-km grid using a drop-in-the-bucket approach. NOAA CRN soil moisture measurements from a 5 cm depth are used to perform a comparison study, and results for stations in Stillwater, OK, USA (SW), and Bowling Green, KY, USA (BG), are described.

Images comparing the high-resolution and low-resolution WARP retrieved soil moisture parameters over North America, along with a zoom-in comparison near Lake Superior, are shown in Fig. 4. Some differences are apparent between retrieved values for m_s, with the high-resolution product exhibiting somewhat greater values of m_s throughout the southeast and southwest U.S. than the WARP product. In the zoom-in comparison, the higher resolution image more clearly resolves the extent of wet areas on the coast of Lake Superior and reveals more of the variation within drier areas.

Differences between the high-resolution and WARP products over North America are further characterized by examining data from 2009. Images of m_s at high-resolution and from the WARP product are processed for every two days using five days of data to reduce coverage gaps. For each pair of high- and low-resolution images, the difference between pixel m_s values is calculated. The mean and standard deviation of the pixel value differences for this period are shown in Fig. 5. The figure demonstrates that the high-resolution m_s estimates exceed those reported by the low-resolution product in some areas throughout North America. Overall, the high-resolution product appears to be slightly biased toward greater values of m_s compared to the low-resolution product. The bias in the high-resolution images may be a result of greater noise levels present in the high-resolution image or in differences in processing techniques. The WARP product may also incorporate more extensive empirical corrections to σ^0_{wet} that are not replicated here, contributing to the differences.

Data from NOAA CRN monitoring stations are also used to assess the performance of the high-resolution product compared to WARP 5.5. For comparison, we use the volumetric soil moisture (m^3/m^3) measurements of the NOAA CRN stations at 5 cm depth. To convert the WARP 5.5 and high-resolution relative moisture percent (m_s) estimates to volumetric soil moisture, we follow the method of Wagner *et al.* [17] and multiply m_s by the soil porosity, where the porosity values are estimated using soil characteristics reported by the Harmonized World Soil Database [24] and equations from Saxton and Rawls [25].

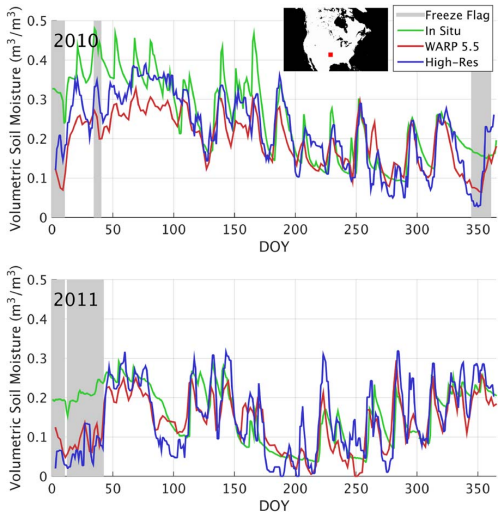

Fig. 6. Time series of volumetric soil moisture versus DOY for 2010 (top) and 2011 (bottom). Plots are shown for *in situ* data from a NOAA CRN station in Stillwater, OK, and from the nearest corresponding grid cell values in the WARP 5.5 and high-resolution data. Measurements which may be contaminated by surface freezing or melt water are indicated by a gray bar.

Time series plots of volumetric soil moisture from the NOAA CRN stations, WARP 5.5, and high-resolution product are shown in Figs. 6 and 7 for 2010 and 2011 for the SW and BG locations. The plotted WARP 5.5 and high-resolution soil moisture values represent a moving five-day average of grid cell values closest in location to the NOAA CRN stations; the averaging reduces estimate noise and produces values at the temporal resolution for which high-resolution images of soil moisture over North America can be produced without significant coverage gaps. Periods where the WARP 5.5 data indicate surface freezing or melt water are indicated by a gray bar.

The plots show that the high-resolution and WARP products demonstrate comparable performance. In some cases, such as the beginning of 2010 for SW, the high-resolution estimates

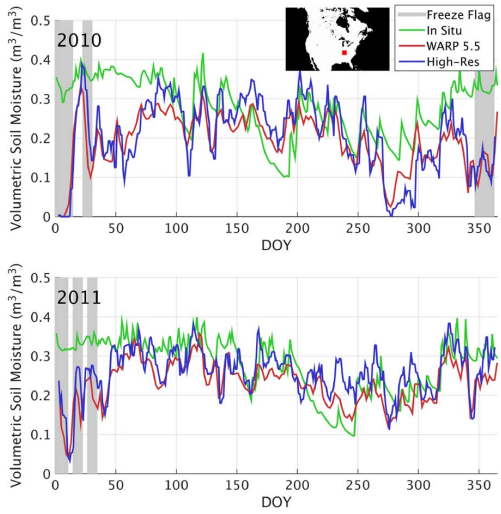

Fig. 7. Time series of volumetric soil moisture versus DOY for 2010 (top) and 2011 (bottom). Plots are shown for *in situ* data from a NOAA CRN station in Bowling Green, KY, and from the nearest corresponding grid cell values in the WARP 5.5 and high-resolution data. Measurements which may be contaminated by surface freezing or melt water are indicated by a gray bar.

TABLE I
TIME SERIES COMPARISON ERROR METRICS

Location	Retrieval Type	R	Bias	RMSE	σ_{err}
SW	WARP 5.5	0.824	-0.032	0.067	0.058
	High-Res	0.824	-0.013	0.060	0.059
BG	WARP 5.5	0.479	-0.054	0.087	0.068
	High-Res	0.331	-0.034	0.093	0.086

better approximate peaks observed in the NOAA CRN *in situ* data. The high-resolution estimates also demonstrate greater variance than WARP 5.5, although this behavior is expected since fewer measurements are used for each grid cell estimate.

A summary of linear regression statistics for the SW and BG two-year time series is shown in Table I for WARP 5.5 and the high-resolution product compared to the *in situ* data. Time series periods flagged in the WARP 5.5 product as contaminated by surface freezing or melt water are omitted from the analysis. The correlation coefficient (R), average bias, root-mean-square error (rmse), and the standard deviation of the error (σ_{err}) are shown and are similar for WARP 5.5 and the high-resolution product in both the SW and BG locations.

The comparable performance of the high-resolution soil moisture estimates to point-scale *in situ* data and WARP 5.5 data suggests that the high-resolution estimates have potential to characterize soil moisture phenomena at a fine scale.

V. CONCLUSION

Using high-resolution estimates of σ^0 produced with ASCAT and the AVE algorithm, soil moisture estimates are produced, which show potential for characterizing fine-scale soil moisture features. Estimates of m_s are produced for North America using a modified version of the TU-Wien algorithm. High-resolution values of m_s show a bias toward greater soil moisture values when compared with the lower resolution WARP soil-moisture product. Time series trends in the high-resolution estimates show a good agreement with the lower resolution product and with point-scale soil moisture measurements from NOAA CRN stations. Although soil moisture retrieval in this letter is limited to North America, retrieval over other regions is possible.

REFERENCES

[1] *Earth Science and Applications From Space: National Imperatives for the Next Decade and Beyond*. Washington, DC, USA: The National Academies Press, 2007.
[2] W. Crow, G. Huffman, R. Bindlish, and T. Jackson, "Improving satellite-based rainfall accumulation estimates using spaceborne surface soil moisture retrievals," *J. Hydrometeorol.*, vol. 10, pp. 199–212, Feb. 2009.
[3] C. Hauck, C. Barthlott, L. Krauss, and N. Kalthoff, "Soil moisture variability and its influence on convective precipitation over complex terrain," *Q. J. R. Meteorol. Soc.*, vol. 137, S1, pp. 42–56, Jan. 2011.
[4] A. L. Barbu, J.-C. Calvet, J.-F. Mahfouf, and S. Lafont, "Integrating ASCAT surface soil moisture and GEOV1 leaf area index into the SURFEX modeling platform: A land data assimilation application over France," *Hydrol. Earth Syst. Sci.*, vol. 18, no. 1, pp. 173–192, Jan. 2014.
[5] A. K. Prasad, L. Chai, R. P. Singh, and M. Kafatos, "Crop yield estimation model for Iowa using remote sensing and surface parameters," *Int. J. Appl. Earth Observ. Geoinf.*, vol. 8, no. 1, pp. 26–33, Jan. 2006.
[6] T. Jackson, M. H. Cosh, R. Bindlish, and J. Du, "Validation of AMSR-E soil moisture algorithms with ground based networks," in *Proc. IEEE IGARSS*, Jul. 2007, pp. 1181–1184.
[7] S. Paloscia, G. Macelloni, E. Santi, and T. Koike, "A multifrequency algorithm for the retrieval of soil moisture on a large scale using microwave data from SMMR and SSM/I satellites," *IEEE Trans. Geosci. Remote Sens.*, vol. 39, no. 8, pp. 1655–1661, Aug. 2001.
[8] S. Hahn, T. Melzer, and W. Wagner, "Error assessment of the initial near real-time MetOp ASCAT surface soil moisture product," *IEEE Trans. Geosci. Remote Sens.*, vol. 50, no. 7, pp. 2556–2565, Jul. 2012.
[9] W. Wagner, G. Lemoine, and H. Rott, "A method for estimating soil moisture from ERS scatterometer and soil data," *Remote Sens. Environ.*, vol. 70, no. 2, pp. 191–207, Nov. 1999.
[10] V. Naeimi, K. Scipal, Z. Bartalis, S. Hasenauer, and W. Wagner, "An improved soil moisture retrieval algorithm for ERS and MetOp scatterometer observations," *IEEE Trans. Geosci. Remote Sens.*, vol. 47, no. 7, pp. 1999–2013, Jul. 2009.
[11] K. Scipal, "Global Soil Moisture Retrieval From ERS Scatterometer Data," Ph.D. dissertation, Inst. Photogramm. Remote Sens. Vienna Univ. Technol., Vienna, Austria 2002.
[12] W. Wagner *et al.*, "The ASCAT soil moisture product: A review of its specifications, validation results, and emerging applications," *Meteorologische Zeitschrift*, vol. 22, no. 1, pp. 5–33, Feb. 2013.
[13] R. D. Lindsley and D. G. Long, "Enhanced-resolution reconstruction of ASCAT backscatter measurements," *IEEE Trans. Geosci. Remote Sens.*, vol. 54, no. 5, pp. 2589–2601, May 2016.
[14] Y. H. Kerr *et al.*, "Soil moisture retrieval from space: The Soil Moisture and Ocean Salinity (SMOS) mission," *IEEE Trans. Geosci. Remote Sens.*, vol. 39, no. 8, pp. 1729–1735, Aug. 2001.
[15] D. Entekhabi *et al.*, "The Soil Moisture Active Passive (SMAP) mission," *Proc. IEEE*, vol. 98, no. 5, pp. 704–716, May 2010.
[16] W. Wagner, S. Hahn, A. Gruber, and W. Dorigo, "Identification of soil moisture retrieval errors: Learning from the comparison of SMOS and ASCAT," in *Proc. IEEE IGARSS*, Jul. 2012, pp. 3795–3798.
[17] W. Wagner *et al.*, "Clarifications on the comparison between SMOS, VUA, ASCAT, and ECMWF soil moisture products over four watersheds in U.S.," *IEEE Trans. Geosci. Remote Sens.*, vol. 52, no. 3, pp. 1901–1906, Mar. 2014.
[18] W. Wagner and G. Lemoine, "Land cover effects on ERS scatterometer data," in *Proc. IEEE IGARSS*, Jul. 1998, vol. 3, pp. 1574–1576.
[19] Scatterometer Climate Record Pathfinder. [Online]. Available: http://www.scp.byu.edu/
[20] R. D. Lindsley, C. Anderson, J. Figa-Saldaña, and D. G. Long, "A parameterized ASCAT measurement spatial response function," *IEEE Trans. Geosci. Remote Sens.*, vol. 54, no. 8, pp. 4570–4579, Aug. 2016, doi: 10.1109/TGRS.2016.2544835.
[21] M. Kottek, J. Grieser, C. Beck, B. Rudolf, and F. Rubel, "World map of the Koppen–Geiger climate classification updated," *Meteorologische Zeitschrift*, vol. 15, no. 3, pp. 259–263, Jun. 2006.
[22] J. E. Bell *et al.*, "U.S. climate reference network soil moisture and temperature observations," *J. Hydrometeorol.*, vol. 14, no. 3, pp. 977–988, Jun. 2013.
[23] H. J. Diamond *et al.*, "U.S. climate reference network after one decade of operations: Status and assessment," *Bull. Amer. Meteorol. Soc.*, vol. 94, no. 4, pp. 489–498, 2013.
[24] FAO/IIASA/ISRIC/ISSCAS/JRC, *Harmonized World Soil Database (Version 1.1)*. Rome, Italy and: FAO, 2009, pp. 1–43.
[25] K. E. Saxton and W. J. Rawls, "Soil water characteristic estimates by texture and organic matter for hydrologic solutions," *Soil Sci. Soc. Amer. J.*, vol. 70, no. 5, pp. 1569–1578, Sep. 2006.